






COMMERCIAL POLYURETHANE CLEAR COAT REINFORCED WITH CARBON NANOTUBES AND HYDROXYAPATITE POWDERS

 Giovanni García-Domínguez¹,  Joan Reyes-Miranda²,
 Geovani Chávez-Escalante¹,  Miguel Ángel Barrón-Meza²,
 Aristeo Garrido-Hernández^{1*}

¹Universidad Tecnológica de Tecámac, Carretera Federal México-Pachuca, Sierra Hermosa, México

²Departamento de Materiales, Área Ciencia de los Materiales, Universidad Autónoma Metropolitana-Azcapotzalco, Av. San Pablo No. 420 Col. Nueva el Rosario C.P. 02128 Alcaldía Azcapotzalco, CDMX

Abstract. Advanced anticorrosive coatings are used in practical applications across various industries, including electronics, biomaterials, automotive and aerospace sectors. Among ceramics, hydroxyapatite (HA) stands out due to its high corrosion resistance and chemical stability. In this study, HA powders were synthesized via the hydrothermal method using calcium nitrate ($\text{Ca}(\text{NO}_3)_2 \cdot 4\text{H}_2\text{O}$) and diammonium hydrogen phosphate ($(\text{NH}_4)_2\text{HPO}_4$), with the addition of surfactants to modulate their morphology. X-ray diffraction analysis confirmed the hexagonal phase of HA with a crystallite size of approximately 20 nm. Scanning electron microscopy (SEM) revealed a nanorod morphology with varying lengths. The HA powders were then blended with multi-walled carbon nanotubes (MWCNTs) poured into a commercial polyurethane clear coat to develop an advanced anticorrosive coating. This composite coating, containing varying loadings of MWCNTs and HA powders, was applied to commercial low-carbon steel (ASTM A1008). Image segmentation analysis quantified the oxide percentage on the coated surfaces. Notably, HA nanorods synthesized using cetyltrimethylammonium bromide (CTAB) as a surfactant and combined with MWCNTs at concentrations of 20 mg HA and 1 mg MWCNTs effectively reduced the oxidation percentage from 28.76% to 4.01%.

Keywords: Hydroxyapatite nanorods, hydrothermal synthesis, polymeric coating, anticorrosive coatings, multi-walled carbon nanotubes.

Corresponding Author: Aristeo Garrido-Hernández, Departamento de Materiales, Área Ciencia de los Materiales, Universidad Autónoma Metropolitana-Azcapotzalco, Av. San Pablo No. 420 Col. Nueva el Rosario C.P. 02128 Alcaldía Azcapotzalco, CDMX, Tel.: 5255-5318-9000; e-mail: agh@azc.uam.mx

Received: 26 August 2024;

Accepted: 11 October 2024;

Published: 10 December 2024.

1. Introduction

Anticorrosive coatings protect metals and alloy surfaces from degradation processes induced by exposure to aggressive fluids, a phenomenon known as corrosion (Ashassi-Sorkhabi *et al.*, 2020). The design of advanced nanocomposites is of significant interest to the industry, as these materials can achieve enhanced physical-chemical performance through the incorporation of micro- and nano-sized reinforcing particles. Ceramics are

How to cite (APA):

García-Domínguez, G., Reyes-Miranda, J., Chávez-Escalante, G., Barrón-Meza, M.A. & Garrido-Hernández, A. (2024). Commercial polyurethane clear coat reinforced with carbon nanotubes and hydroxyapatite powders. *New Materials, Compounds and Applications*, 8(3), 343-354 <https://doi.org/10.62476/nmca83343>

often preferred for corrosion resistance due to their inherent chemical stability. One such ceramic compound is hydroxyapatite (HA, $\text{Ca}_{10}(\text{PO}_4)_6(\text{OH})_2$), which is recognized for its exceptional corrosion-resistant properties. HA's effectiveness as an anticorrosive material is further enhanced by controlling its particle size and morphology, which can be achieved using various synthesis methods. Among these methods, wet chemical techniques are particularly favored for producing specific morphologies and particle sizes. The ability to tailor HA particles through these methods has made HA a promising candidate for anticorrosion applications in various industries, including biomedical, automotive and aerospace sectors (Qi *et al.*, 2016).

The hydrothermal method enables the synthesis of hydroxyapatite crystals with precise control over their sizes and shapes (Alif *et al.*, 2018). Various morphologies of HA, such as nanowires, nanoribbons, spheres and prisms, have been successfully produced using this technique (Sadat-Shojai *et al.*, 2013). Šimková *et al.* (2018) demonstrated that the crystallite and particle size of HA markedly affected the anticorrosive properties and concluded that smaller needle-shaped particles possess better anticorrosive efficiency. Utilizing different particle sizes and morphologies of HA has proven advantageous in combination with polyurethane (PU), which is an excellent candidate for anticorrosive coatings (Mohammadi *et al.*, 2018). Lin *et al.* (2019) developed a porous elastomer based on PU reinforced with HA particles for plastic reconstruction applications, which exhibited a uniform pore structure and sufficient strength to withstand general pressure and tensile stress. Additionally, a composite coating incorporating functionalized graphene oxide (GO) in a polyurethane matrix has been elaborated, showing promising anticorrosive properties as characterized by electrochemical impedance spectroscopy (EIS) and salt spray tests (Zhang *et al.*, 2020). EIS results indicated no undercoating corrosion occurred after 235 hours of immersion in an electrolyte solution containing 3.5 wt% NaCl. This demonstrates the coating's effectiveness in preventing corrosion over an extended period. Additionally, the incorporation of multi-walled carbon nanotubes (MWCNTs), known for their high tensile strength and elastic modulus, allows for the reinforcement of polymers (Zhang *et al.*, 2020).

Recent studies have shown that functionalizing carbon nanotubes can significantly enhance the mechanical properties of polymeric materials (Coleman *et al.*, 2006). For instance, reinforcing a polymer matrix with just 1 wt% of CNTs can increase the composite's stiffness by 36-42% and its tensile strength by approximately 25%. Based on this, it follows that combining hydroxyapatite (HA) with CNTs could result in a highly effective anticorrosive coating. Li *et al.* (2017) highlighted the potential benefits of such a combination, suggesting that the synergy between HA's corrosion resistance and CNTs' mechanical reinforcement could lead to advanced coatings with superior performance.

In the field of coatings, a critical challenge is calculating the damage caused by corrosion and predicting the remaining useful life of exposed products. An accurate assessment of corrosion damage is essential for maintaining the integrity and longevity of materials. Lebrun *et al.* (2000) quantified corrosion damage through color alteration, providing a visual method to assess degradation. Gelli *et al.* (2003) developed an automated approach known as the "Shading Method Form" to reconstruct degraded stone surfaces, demonstrating the potential of automation in damage assessment. Boukouvalas *et al.* (1998) introduced computer vision techniques for detecting and classifying mineral streaks in ceramic tiles, showcasing the application of advanced imaging technology in material analysis. Further investigations have explored the use of artificial vision systems

to obtain high-resolution images of corrosion damage (Lee *et al.*, 2009). These systems provide detailed visual data on oxidation-induced degradation, enhancing the accuracy of damage assessment. However, their use is often limited by the need for human intervention to operate the technology effectively.

Preparing the coating base in commercial polyurethane coats with HA and MWCNTs load is low-cost. The nanotubes create a barrier that blocks corrosive agents like water and oxygen, while HA's high chemical stability further strengthens the coating. Together, they reduce oxide formation on metal surfaces, protecting underlying materials like carbon steel from oxidation. This coating will increase its durability in industrial environments exposed to aggressive substances.

The present investigation used hydroxyapatite (HA) nanorods and multi-walled carbon nanotubes (MWCNTs) to reinforce polyurethane clear coatings. These coatings were deposited on commercial low-carbon steel (ASTM A1008) sheets using the tape casting technique. The combination of HA and MWCNTs in the polyurethane matrix aimed to enhance the anticorrosive properties and mechanical strength of the coatings. This study underscores the potential of advanced nanocomposites in extending the service life of materials exposed to corrosive environments, contributing to more durable and reliable protective coatings.

2. Experimental

2.1. Materials

The starting materials used for the synthesis included calcium nitrate tetrahydrate ($\text{Ca}(\text{NO}_3)_2 \cdot 4\text{H}_2\text{O}$, Mallinckrodt, 99%), di-ammonium hydrogen phosphate ($(\text{NH}_4)_2\text{HPO}_4$, Baker Analyzed, 98.7%) and deionized water. Cetyltrimethylammonium bromide (CTAB, ACS reagent, $\geq 99.0\%$) and sodium dodecyl sulfate (SDS, ReagentPlus®, $\geq 98.5\%$) were employed as surfactants. Solutions of $\text{Ca}(\text{NO}_3)_2$ and $(\text{NH}_4)_2\text{HPO}_4$ were prepared at specific molar concentrations using deionized water. The volumes used ensured a Ca/P ratio of 1.67, corresponding to the stoichiometric ratio for hydroxyapatite (HA).

2.2. Synthesis Procedure

For the HA-CTAB synthesis, 0.01 mol of CTAB was dissolved in a 0.5 M $\text{Ca}(\text{NO}_3)_2$ solution. For the HA-SDS synthesis, 0.001 M of SDS was used. Both solutions were stirred at 50°C and 600 rpm for 20 minutes to ensure complete dissolution of the surfactants. The $(\text{NH}_4)_2\text{HPO}_4$ solution was added dropwise to the $\text{Ca}(\text{NO}_3)_2$ solution, with continuous stirring at 50°C. The pH of the mixture was adjusted to 11 by adding 1.5 M NaOH. After complete addition, the mixed solution was maintained under stirring for an additional 30 minutes. The resulting milky suspension was transferred to a Teflon® container, hermetically sealed and heated in an oven at 200°C for 15 hours. The precipitate was then washed three times with deionized water using centrifugation at 10,000 rpm for 15 minutes per wash to remove any residual CTAB and SDS. The washed powders were dried at 120°C for 8 hours.

2.3. Multi-walled carbon nanotubes dispersion

The multi-walled carbon nanotubes, MWCNTs, were treated with a solution of nitric acid (HNO_3) (89%) and sulfuric acid (H_2SO_4) (91%) in a volume ratio of 3:1.

Initially, the MWCNTs were sonicated in distilled water at room temperature for 30 minutes. Subsequently, the MWCNTs were dispersed in the acid solution for 120 minutes at room temperature. After the acid treatment, the MWCNTs were rinsed with distilled water and dried at 120°C for 8 hours.

2.4. Polymeric coating procedure

Commercial low-carbon steel ASTM A1008, composed of Fe 99.39%, Mn 0.5%, C 0.1%, S 0.005% and P 0.004% by weight, was used as the substrate. The ASTM A1008 specimens were first cut into 70 mm x 140 mm dimensions. They were then sanded sequentially with 180, 120, 25 and 20 μm grit sandpaper and cleaned with ethanol to prepare for coating. The polymeric coatings reinforced with hydroxyapatite (HA) and MWCNTs were prepared as follows: the reference polymeric coating (P) consisted solely of commercial polyurethane clear coat (CPCC, Sherwin Williams®). Polymeric coatings containing HA synthesized without surfactants, with CTAB surfactant and with SDS surfactant were designated as PH, PHC and PHS, respectively. When the polymeric coating also contained MWCNTs, an “M” was added to the sample code.

The reinforced polymeric coatings described in Table 1 include, for example, the sample PHC2M, which contains 20 mg of hydroxyapatite synthesized using CTAB and 1 mg of MWCNTs dispersed in 2000 mg of CPC. This corresponds to 1 wt% of HA and 0.05 wt% of MWCNTs based on the total weight of the CPCC polymer. The CTP-catalyst mixture was prepared according to the manufacturer's instructions. The MWCNTs and HA powders were thoroughly dispersed in the polymer using an ultrasonic bath before adding the catalyst. Finally, several substrate sheets were coated with the prepared mixture. The coating was applied in a single layer, with its thickness controlled to be approximately 0.1 mm. The coatings were prepared in duplicate.

Table 1 summarizes the compositions of the reinforced polymeric coatings. Testing sheets were exposed for 30 days to the corrosive environment (2M NaOH solution) at room temperature. All experiments were performed simultaneously in a 5-liter container containing 3 liters of [2 M] NaOH solution, ensuring that all samples were placed equidistant from the walls and from each other. The coating did not touch the solution.

The NaOH solution was used to create an artificial atmosphere to promote polymer degradation and oxidation of the 1020 steel substrate. Exposure to the solution lasted for 30 days and the experiments were duplicated. The volume-surface ratio was kept constant based on this configuration. The results were consistent across both sets of experiments, validating the reproducibility of the setup.

Table 1. Composition of HA and MWCNTs in CPC coatings on ASTM 1008 steel substrate

Sample	HA (mg)	Surfactant	MWCNTs (mg)
S*	----	----	----
P	----	---	----
PH	10	---	---
PHM	10	---	0.5
PHSM	10	SDS	0.5
PHCM	10	CTAB	0.5
PHS2M	20	SDS	1
PHC2M	20	CTAB	1

2.5. Oxidation area determination of polymeric coating

To determine the iron oxide content in the polymeric coating, a total coated area of 78 cm² was analyzed. The methodology involved image segmentation using ImageJ software. The red regions, corresponding to iron oxide, were isolated by adjusting the color threshold to highlight these areas. This approach allowed for the precise quantification of the iron oxide-covered surface. Simultaneously, the blue regions, representing the polymeric coating without oxide, were also segmented. The sum of the red and blue areas accounted for 100% of the total polymeric coating surface. The percentage of iron oxide in the coating was calculated by dividing the area corresponding to the red regions (iron oxide) by the total coating area, yielding the proportion of the surface occupied by iron oxide.

2.6. HA and MWCNTs characterization

The Fourier transform infrared spectroscopy (FT-IR) was performed using a Perkin-Elmer Spectrum two spectrophotometer. The spectrum was recorded at 32 scans in the 4000-450 cm⁻¹ range. Identification of the crystalline phases of the powders was carried out by X-ray diffraction (XRD) at room temperature using a Bruker d8 advance echo diffractometer with incident Cu K α radiation ($\lambda = 1.54184 \text{ \AA}$), in the 2θ range of 20 to 55°. The morphological features of powders were investigated with a JOEL scanning electron microscope model JSM-6000 operating under a high vacuum and low accelerating voltage of 5 kV. Thermal stability tests were made by thermogravimetric analysis using a TA instruments model SDT Q600 kit from 25 to 1000°C with a heating ramp of 20°C/min.

3. Results and discussion

Figure 1 presents the FT-IR spectra of the HA samples. Absorption bands corresponding to the surfactants were not detected, indicating their effective removal during the washing stage. The broad FT-IR band centered approximately at 1091 cm⁻¹ corresponds to the asymmetric stretch vibration mode of the PO₄³⁻ group. The band at 550 cm⁻¹ corresponds to the symmetric P-O stretching vibration of the PO₄³⁻ group. The band at 630 cm⁻¹, corresponding to the OH⁻ group, is related to absorbed water (Varma *et al.*, 2005; Rocha *et al.*, 2005).

The FT-IR spectra depicted in Figure 1 (blue line) correspond to the MWNTs, displaying characteristic absorption bands. Notably, the C-H stretching vibrations associated with sp² and sp³ hybridized carbon-hydrogen bonds are observed at 2916 and 2850 cm⁻¹. Additionally, the C-O stretching vibrations appear in the range of 1300–1000 cm⁻¹, which are linked to the presence of ether, alcohol or ester groups commonly associated with functionalized MWNTs. The absorption band located around 1226 cm⁻¹ is consistent with the C-O stretching vibrations in the MWNT samples (Misra *et al.*, 2005; Stobinski *et al.*, 2010).

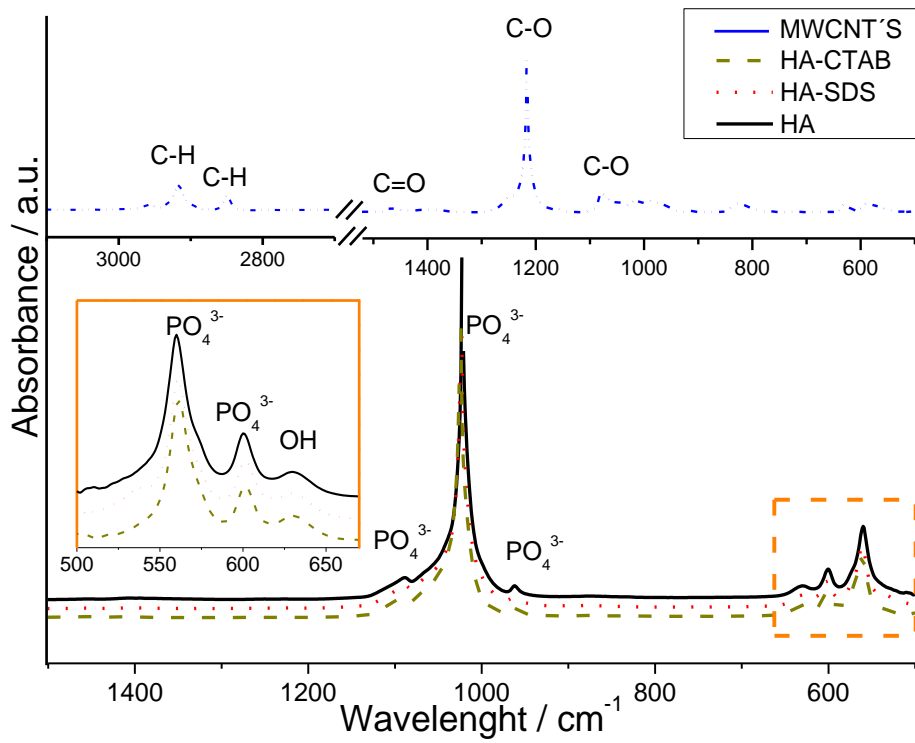


Figure 1. FT-IR spectra of HA, HA-CTAB, HA-SDS and MWCNT

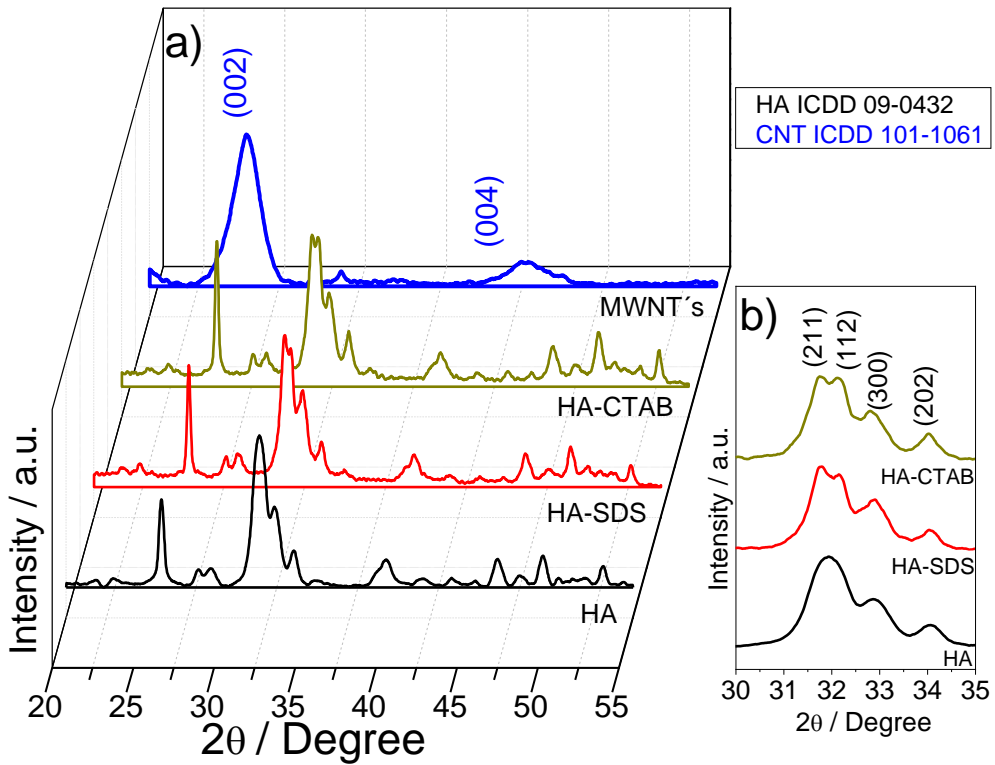


Figure 2. XRD patterns of HA powders synthesized using surfactant

The XRD patterns of the synthesized samples are shown in Figure 2a and b. The peak positions are in good agreement with the JCPDS (09-0432) standard, which corresponds to hydroxyapatite (HA) with lattice parameters $a \approx b \approx 0.9418$ nm, $c \approx 0.6884$ nm and space group P63/m. This confirms that standard HA with a hexagonal structure was formed during synthesis. The XRD pattern exhibits narrow peaks, indicating good crystallinity.

In Figure 2b, the peak located around $2\theta = 32.2^\circ$ corresponds to the (112) plane. Narrower peaks were observed in the HA samples synthesized with surfactants (HA-CTAB and HA-SDS), indicating higher crystallinity compared to the standard HA sample. This difference can be attributed to the modification of surface tension, which enhances the dispersion of Ca ions.

No secondary crystalline phases were observed. Figure 2a shows the XRD patterns of MWCNTs. The peak at $2\theta = 26^\circ$ corresponds to the (002) plane, matching the concentric graphene sheets of the MWCNTs (Li *et al.*, 2009; Osikoya *et al.*, 2015). The width and intensity of the (002) and (004) planes are related to the number of layers in the nanotubes (Tascón *et al.*, 2007; Shen *et al.*, 2007). The crystallite size of the HA powder was determined using the Scherrer Equation (1):

$$L = \frac{K \lambda}{\beta \cos\theta}, \quad (1)$$

where L is the average crystallite size, λ is the X-ray wavelength in nanometers (nm), β is the peak width at half maximum height in radians and K is a constant related to particle shape, usually taken as 0.9, θ is the Bragg angle. The crystallite sizes were found to be 19.89 nm, 20.58 nm and 21.32 nm for HA, HA-CTAB and HA-SDS, respectively. The presence of the (211) and (202) planes indicates that the crystallites are very small (Sadat-Shojai *et al.*, 2010).

The micrographs of the HA powders synthesized by the solvothermal method are shown in Figure 3. The morphology of the hydroxyapatite powders consisted of nanorods exhibiting similar length-to-diameter ratios across the samples. The calculated ratios were 3.27 ± 0.99 , 3.38 ± 1.36 and 2.88 ± 1.04 for HA, CTAB+ and SDS+, respectively (Previous experimentation reported these values, (García-Domínguez *et al.*, 2021)). This difference in length is attributed to the nucleation mechanism induced by the surfactant. Bricha *et al.* (2012) studied the behavior of different surfactants in preparing HA and their influence on the nucleation process and crystal growth. They found that the HA particles initially formed as fibrous polycrystals, which converted into nanorods with uniform morphology after hydrothermal treatment.

Blending particles with a rod-like morphology as a reinforcing agent in the polymer matrix results in the formation of complex networks within the polymers (Scotti *et al.*, 2014). The HA samples were evaluated using thermogravimetric (TGA) and differential thermal analyses (DTA). Figure 4 shows the thermogravimetric curve of HA powder heated from room temperature to 1000°C. In the temperature range of 100-400°C, the HA-SDS powders lost 4.21 wt%, the HA-CTAB powders lost 2.93 wt% and the HA lost 1.72 wt%. This weight loss corresponds to the evaporation of water adsorbed on the surface and within the pores.

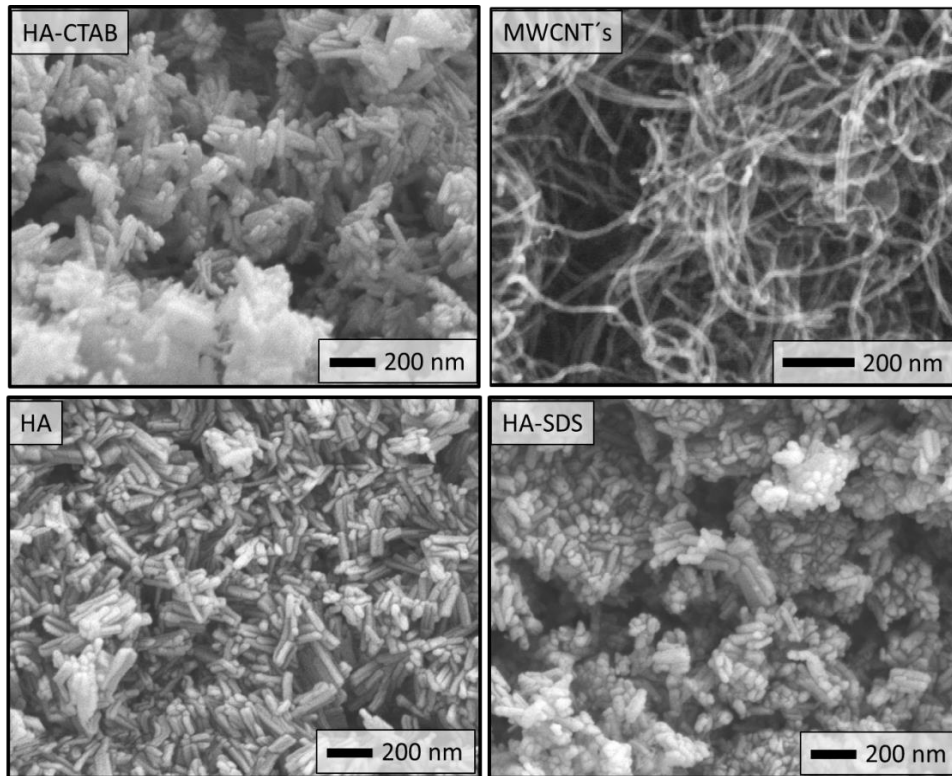


Figure 3. SEM micrographs of HA, HA-CTAB, HA-SDS and MWCNTs of studied specimens

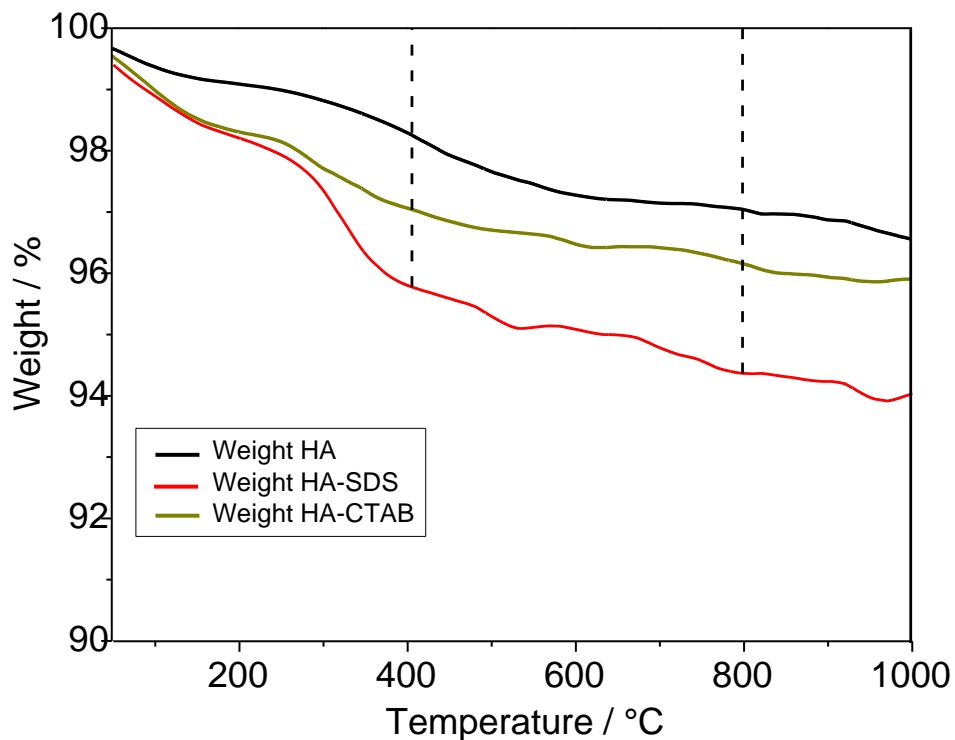


Figure 4. Thermogravimetric curve of HA powders

A smaller weight loss was observed in the 400–800 °C range, with the HA-SDS sample losing 1.46 wt% and the HA-CTAB sample losing 0.89 wt%. This loss is

attributed to chemically adsorbed water molecules. Between 800 and 1000 °C, the HA-SDS sample lost 0.36 wt%, while the HA-CTAB sample lost 0.25 wt%, which is associated with the transformation of hydroxyapatite (HA) into tricalcium phosphate ($\text{Ca}_3(\text{PO}_4)_2$, β -TCP) (Khayrutdinova *et al.*, 2023).

The hydroxyapatite powders synthesized with the surfactants CTAB and SDS showed greater weight loss at 400°C, due to the thermal decomposition of surfactant residues that remained trapped in or adsorbed on the particle surfaces. Although the hydroxyapatite powders were washed, the use of CTAB and SDS during synthesis influenced their stability at high temperatures. After removing organic material, the weight/temperature slope in the 400-800°C range was similar to that of HA synthesized without surfactants. The higher weight loss observed in HA synthesized using CTAB and SDS does not necessarily negatively impact coating performance; subsequent results indicate that these HA powders effectively reduced the oxidation area.

The coated steel sheets were exposed to a corrosive environment for 30 days in a NaOH solution. The control steel sheet exhibited significant oxidation. As expected, the “P” sample demonstrated lower corrosion than the “S” sample (Table 1). All coated steel sheets with PU and different loadings of HA and MWCNTs exhibited varying oxidation areas. Souza *et al.* (2018) coated ASTM A1008 steel sheets using polystyrene and showed that coatings with a thickness of 40 μm resisted corrosion effectively. By controlling the coating thickness, the extent of corrosion attack can be managed. To analyze the images of the samples, they were processed by segmentation, dividing the digital image into several groups of pixels or objects to simplify the representation of the image. The polymeric coating on the ASTM 1008 steel sheet was segmented using image processing software, with oxidized areas highlighted in red for precise measurement. This method enabled accurate oxidation quantification, primarily occurring at the coating edges, likely at the adhesion zones. The segmentation of the coated steel sheets is shown in Figure 5. Segmentation was focused on the coated area to minimize noise in the analysis. The results are summarized in Table 2.

Table 2. Percentage of surface oxidation according to segmentation with Trainable Segmentation

Sample	Oxidation percentage %
S	88.59
P	28.76
PH	19.95
PHM	14.54
PHSM	13.36
PHCM	12.58
PHSM2	8.42
PHCM2	4.01

In this study, the uncoated sample exhibited the most corrosion damage, with degradation primarily occurring at the edges. The lack of adherence of the polymer further promoted oxidation. The PH sample showed 19.95% oxidation damage, while the PHM specimen reduced this damage to 14.54%. This result indicates the contribution of MWCNTs to the HA powders, enhancing the interaction between the coating and the

substrate (Zhang *et al.*, 2015). The polymeric coating containing the HA powder synthesized with CTAB (PHCM and PHCM2 samples) exhibited less corrosion than their counterparts synthesized with SDS (PHSM and PHSM2 samples) regardless of the concentration of HA used in the polymeric coating. The difference in oxidation protection levels among the tested coating materials is attributed to the particles' surface energy, which improves the polymer's adherence.

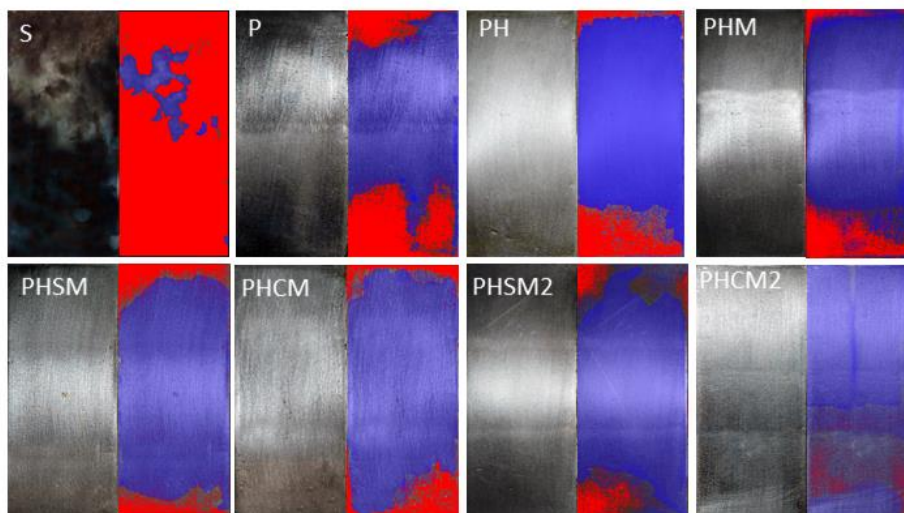


Figure 6. Segmentation of ASTM A1008 commercial steel sheet coated and treated (The blue color indicates the oxidized area, while the blue region represents areas free of oxidation)

4. Conclusion

In this study, ASTM A1008 steel sheets were coated with a commercial polyurethane clear coat, reinforced with HA powders and MWCNTs (0.5 and 1 wt% of HA and 0.025 wt% of MWCNTs based on the total weight of the polyurethane clear coat). The HA nanorods, successfully synthesized via a surfactant-assisted hydrothermal method, exhibited crystallite sizes in the nanometer range. Coatings reinforced with HA nanorods synthesized with CTAB reduced oxidation to 28.76% of the exposed area. This reinforcement significantly improved the adhesion of the coating, effectively enhancing corrosion resistance. These findings highlight the potential of HA nanorod-reinforced coatings in protecting ASTM A1008 steel sheets from corrosion.

Acknowledgments

The authors gratefully acknowledge UAM-Azcapotzalco and CCAI-UTTEC for the use of the facilities and the characterization analyses.

References

- Alif, M.F., Aprillia, W. & Arief, S. (2018). A hydrothermal synthesis of natural hydroxyapatite obtained from *Corbicula moltkiana* freshwater clams shell biowaste. *Materials Letters*, 230, 40-43.
- Ashassi-Sorkhabi, H., Kazempour, A. (2020). Incorporation of organic/inorganic materials into polypyrrole matrix to reinforce its anticorrosive properties for the protection of steel alloys: A review. *Journal of Molecular Liquids*, 309, 113085.

- Boukouvalas, C., De Natale, F., De Toni, G., Kittler, J., Marik, R., Mirmehdi, M., Petrou, M., Le Roy, P., Salgari, R. & Vernazza, G. (1998). ASSIST: Automatic system for surface inspection and sorting of tiles. *Journal of Materials Processing Technology*, 82(1-3), 179-188.
- Bricha, M., Belmamouni, Y., Essassi, E.M., Ferreira, J.M. & Mabrouk, K.E. (2012). Surfactant-assisted hydrothermal synthesis of hydroxyapatite nanopowders. *Journal of Nanoscience and Nanotechnology*, 12(10), 8042-8049.
- Coleman, J.N., Khan, U. & Gun'ko, Y.K. (2006). Mechanical reinforcement of polymers using carbon nanotubes. *Advanced Materials*, 18(6), 689-706.
- García-Domínguez, G., Diaz De La Torre, S., Chávez-Güitrón, L., Vergara-Hernández, E., Reyes-Miranda, J., Quezada-Cruz, M. & Garrido-Hernández, A. (2021). Effect of the structural and morphological properties of surfactant-assisted hydroxyapatite on dermal irritation and antibacterial activity. *Materials*, 14, 6522.
- Gelli, D., Vitulano, D. (2003). Speed up of shape from shading using graduated non-convexity. In *Discrete Geometry for Computer Imagery: 11th International Conference*, Naples, Italy, 504-513. Springer Berlin Heidelberg.
- Khayrutdinova, D.R., Goldberg, M.A., Antonova, O.S., Kroklicheva, P.A., Fomin, A.S., Obolkina, T.O., Konovalov, A.A., Akhmedova, S.A., Sviridova, I.K. & Kirsanova, V.A. (2023). Effects of heat treatment on phase formation in cytocompatible sulphate-containing tricalcium phosphate materials. *Minerals*, 13, 147.
- Lebrun, V., Toussaint, C. & Pirard, E. (2000). The use of image analysis for quantitative monitoring of stone alteration. In *Stone Decay its Causes and Controls*.
- Lee, J.S., Hwang, I., Hyun Hong, S. & Seok Lee, H. (2009). Advanced robot system for automated bridge inspection and monitoring. In *IABSE Symposium: Sustainable Infrastructure-Environment Friendly, Safe and Resource Efficient*, Bangkok, Thailand, 45-52.
- Li, H., Song, X., Li, B., Kang, J., Liang, C., Wang, H. & Qiao, Z. (2017). Carbon nanotube-reinforced mesoporous hydroxyapatite composites with excellent mechanical and biological properties for bone replacement material application. *Materials Science and Engineering: C*, 77, 1078-1087.
- Li, Q., Viereckl, A., Rottmair, C.A. & Singer, R.F. (2009). Improved processing of carbon nanotube/magnesium alloy composites. *Composites Science and Technology*, 69(7-8), 1193-1199.
- Lin, L., Chang, Z. & Ding, G. (2019). Resuspension of deposited nanoparticles during pool boiling. *International Journal of Heat and Mass Transfer*, 130, 230-239.
- Misra, A., Tyagi, P.K., Singh, M.K. & Misra, D.S. (2006). FTIR studies of nitrogen doped carbon nanotubes. *Diamond and Related Materials*, 15(2-3), 385-388.
- Mohammadi, A., Barikani, M., Doctorsafaei, A.H., Isfahani, A.P., Shams, E. & Ghalei, B. (2018). Aqueous dispersion of polyurethane nanocomposites based on calix arenes modified graphene oxide nanosheets: Preparation, characterization and anti-corrosion properties. *Chemical Engineering Journal*, 349, 466-480.
- Osikoya, A.O., Wankasi, D., Vala, R.M.K., Dikio, C.W., Afolabi, A.O., Ayawei, N. & Dikio, E.D. (2015). Synthesis, characterization and sorption studies of nitrogen-doped carbon nanotubes. *Digest Journal of Nanomaterials and Biostructures*, 10(1), 125-134.
- Qi, M.L., Xiao, G.Y. & Lu, Y.P. (2016). Rapid hydrothermal synthesis of submillimeter ultralong flexible hydroxyapatite fiber using different pH regulators. *Acta Metallurgica Sinica (English Letters)*, 29, 609-613.
- Rocha, J.H.G., Lemos, A.F., Agathopoulos, S., Valério, P., Kannan, S., Oktar, F.N. & Ferreira, J.M.F. (2005). *Scaffolds for bone restoration from cuttlefish*. *Bone*, 37(6), 850-857.
- Sadat-Shojai, M., Atai, M., Nodehi, A. & Khanlar, L.N. (2010). Hydroxyapatite nanorods as novel fillers for improving the properties of dental adhesives: Synthesis and application. *Dental Materials*, 26(5), 471-482.

- Sadat-Shojai, M., Khorasani, M.T., Dinpanah-Khoshdargi, E. & Jamshidi, A. (2013). Synthesis methods for nanosized hydroxyapatite with diverse structures. *Acta Biomaterialia*, 9(8), 7591-7621.
- Scotti, R., Conzatti, L., D'Arienzo, M., Di Credico, B., Giannini, L., Hanel, T., Stagnaro, P., Susanna, A., Tadiello, L., Morazzoni, F. (2014). Shape controlled spherical (0D) and rod-like (1D) silica nanoparticles in silica/styrene butadiene rubber nanocomposites: Role of the particle morphology on the filler reinforcing effect. *Polymer*, 55(6), 1497-1506.
- Shen, J., Huang, W., Wu, L., Hu, Y. & Ye, M. (2007). The reinforcement role of different amino-functionalized multi-walled carbon nanotubes in epoxy nanocomposites. *Composites Science and Technology*, 67(15-16), 3041-3050.
- Šimková, L., Šulcová, P. (2018). Synthesis and characterization of hydroxyapatite for anticorrosion purposes. In *Proceedings of the 6th International Conference on Chemical Technology*. Česká společnost průmyslové chemie.
- Souza, C.D., Teixeira, R.L.P., Lacerda, J.C.D., Ferreira, C.R., Teixeira, C.H.B.S. & Signoretti, V.T. (2018). Polystyrene and cornstarch anti-corrosive coatings on steel. *Polímeros*, 28(3), 226-230.
- Stobinski, L., Lesiak, B., Kövér, L., Tóth, J., Biniak, S., Trykowski, G. & Judek, J. (2010). Multiwall carbon nanotubes purification and oxidation by nitric acid studied by the FTIR and electron spectroscopy methods. *Journal of Alloys and Compounds*, 501(1), 77-84.
- Tascón, J.M. (2007). Carbon materials: Their structures and types. *Óptica Pura Y Aplicad*, 40(2), 149-159.
- Varma, H.K., Babu, S.S. (2005). Synthesis of calcium phosphate bioceramics by citrate gel pyrolysis method. *Ceramics International*, 31(1), 109-114.
- Zhang, F., Liu, W., Liang, L., Wang, S., Shi, H., Xie, Y. & Pi, K. (2020). The effect of functional graphene oxide nanoparticles on corrosion resistance of waterborne polyurethane. *Colloids and Surfaces A: Physicochemical and Engineering Aspects*, 591, 124565.
- Zhang, Y., Dong, Y. (2015). Effect of surfactant on morphology of hydroxyapatite. *Synthesis and Reactivity in Inorganic, Metal-Organic and Nano-Metal Chemistry*, 45(3), 411-414.